Journal of Water Process Engineering 68 (2024) 106520

Contents lists available at ScienceDirect

Journal of Water Process Engineering

journal homepage: www.elsevier.com/locate/jwpe

Bimetallic MOF sulfurized In_2S_3/Fe_3S_4 for efficient photo-Fenton degradation of atrazine under weak sunlight: Mechanism insight and degradation pathways

Hong-Ming Zhang, Shu-Ting Cheng, Xiao-Fang Shen, Yue-Hong Pang [*]

School of Food Science and Technology, Jiangnan University, Wuxi 214122, China

ARTICLE INFO

Editor: Jing Zhang

Keywords:
Atrazine
Sulfurization
In_2S_3/Fe_3S_4
Photo-Fenton
Sunlight-driven

ABSTRACT

Atrazine (ATZ) permeates into aquatic environments due to agricultural activities, presenting potential health risks and necessitating effective degradation strategies. In this paper, bimetallic MOF MIL-68(In/Fe) sulfurized heterostructured In_2S_3/Fe_3S_4 (M-ISFS) was synthesized successfully by a two-step solvothermal reaction. M-ISFS demonstrated ample Fe sites, facilitating the Fenton reaction. The heterostructures facilitated electron transfer in M-ISFS, resulting in a significant acceleration of the reduction of Fe^{3+}. M-ISFS demonstrated an efficient degradation capacity ATZ (99.6 % in 60 min), under a low catalyst dosage (0.15 $g \cdot L^{-1}$) and weak sunlight intensity (26.79 $mW \cdot cm^{-2}$). It also retained 88.7 % degradation efficiency after undergoing 4 cycles. $^1O_2$, $\cdot OH$ and $\cdot O_2^-$ were identified to be the main reactive species in the photo-Fenton reaction. The detailed degradation mechanism and pathway were investigated via mass spectrometry (MS) and density functional theory (DFT). Toxicity assessment of intermediates showed that M-ISFS-mediated photo-Fenton degradation attenuates ATZ toxicity to aquatic organisms. This study will broaden the utilization of catalysts sulfurized from MOFs for improving photo-Fenton degradation.

1. Introduction

The expansion of global agricultural production led to a rise in the application of herbicides, which has in turn increased the aquatic environment contamination and the potential harm to humans. Atrazine (ATZ) is a widely used broad-spectrum herbicide with its 2019 use exceeding 70 million pounds in the United States alone [1]. It has been found to be potentially harmful to humans such as altering testosterone levels, reducing sperm quality and affecting fetal development, which has been classified as one of the endocrine disrupting chemicals [2–4]. ATZ is more persistent and bioaccumulative than many other herbicides, with a half-live of up to 57 weeks in different matrices [5]. Alarming levels of ATZ have been found in lake [6], drinking water [7] and fish [8], posing a considerable risk to human health. Hence, an efficient method for the degradation of ATZ in aquatic environments is crucial.

The Fenton process has been identified as a straightforward and effective technique for the degradation of contaminations in aqueous environments [9]. However, traditional Fenton process is limited by its narrow pH operating range, excessive H_2O_2 consumption, and the generation of iron sludge [10]. The utilization of the heterogeneous photo-Fenton process offers a potential solution to the aforementioned challenges by enabling the effective harnessing of solar energy through the use of catalysts, leading to decreased consumption of H_2O_2 and minimized formation of iron sludge [11]. Moya [12] et al. explored the conventional Fenton degradation of sulfamethazine and the results showed that less than 20 % of the total organic carbon (TOC) was degraded in 60 min. However, for the same concentration of sulfamethazine, Chen's [13] study showed that heterogeneous photo-Fenton process can degrade more than 50 % of TOC in 30 min. In heterogeneous photo-Fenton reactions, catalysts play a crucial role in promoting carrier separation by absorbing sunlight, thereby regulating the Fe^{3+}/Fe^{2+} cycle and the generation of reactive species [14]. Nevertheless, the recombination of photogenerated carriers can pose a significant hindrance [15]. Therefore, developing high-performance photo-Fenton catalysts hinges on the effective separation of carriers and the mitigation of their recombination.

Metal-organic frameworks (MOFs), consisting of metal centers and organic ligands, have shown significant promise in the development of photo-Fenton catalysts [16,17]. MOFs generally exhibit semiconductor-like characteristics, enabling them to be excited by light to generate

---

[*] Corresponding author.
E-mail address: yhpang@jiangnan.edu.cn (Y.-H. Pang).

https://doi.org/10.1016/j.jwpe.2024.106520
Received 17 July 2024; Received in revised form 16 October 2024; Accepted 6 November 2024

photogenerated electrons and holes [18]. However, the limited photoactivity of basic MOFs hinders the efficient utilization of these photogenerated carriers, necessitating modification [19]. Utilizing MOFs as templates, the derivatization process has been proven to be an effective strategy in addressing this issue [20]. MOFs can be derivatized by multiple routes to form various oxides [21], sulfides [22], or phosphide [23]. These derivatives exhibit enhanced photoactivity while retaining the fundamental properties of MOF. Additionally, the inherent flexibility of MOFs enables convenient adjustment of the metal components for the desired derivatives, which is propitious to the construction of heterostructures. Thus, catalysts derived from bimetallic MOFs possess ample catalytic sites, improved light absorption properties and effective separation of photogenerated carrier [24]. Thus, the selection of the precursor MOF metal element and the derivatization method is crucial for the synthesis of heterostructured photo-Fenton catalysts.

Metallic sulfides are commonly utilized in the design of heterostructures owing to its superior photosensitivity, appropriate energy band structure, and exceptional charge mobility characteristics [25]. These heterostructured sulfide-based materials demonstrate exceptional performance in energy [26], environmental [27] and sensing [28] applications. Among the numerous metal sulfides, In_2S_3 is utilized in the degradation of contaminants due to its relatively low toxicity compared to most sulfides [29]. Yan [30] et al. synthesized heterostructured In_2S_3/Bi_2WO_6, which enhanced the separation and transfer of photogenerated carriers, 2–3-times enhancing the degradation rate. Thus, In_2S_3-containing heterostructures by sulfuring MOF have potential in enhancing photo-Fenton degradation.

Herein, bimetallic MOF MIL-68(In/Fe) sulfurized heterostructured In_2S_3/Fe_3S_4 (M-ISFS) was synthesized successfully by a two-step solvothermal reaction for the degradation of the herbicide ATZ under a weak sunlight-driven photo-Fenton reaction. The morphology, elemental and chemical structure of M-ISFS was characterized via scanning electron microscopy (SEM), X-ray diffractometer (XRD) and X-ray photoelectron spectroscopy (XPS). Optical and electronic properties of M-ISFS were analyzed through electrochemical workstation. A comprehensive investigation was conducted into the degradation properties, influencing factors and practical applications of M-ISFS. The degradation mechanism of the system, the degradation pathway of ATZ and the toxicity of intermediates were also analyzed.

2. Experimental sections

2.1. Chemicals and reagents

The detailed information of chemicals and regents was provided in Text S1.

2.2. Synthesis of MIL-68(In/Fe)

MIL-68(In/Fe) was synthesized according to the method reported in the literature [31] with some modifications. Typically, 270 mg of $FeCl_3 \cdot 6H_2O$, 902 mg of $In(NO_3)_3 \cdot xH_2O$ and 664 mg of p-phthalic acid (PTA) were added into 20 mL of N,N-dimethylformamide (DMF). The mixed solution was stirred and ultrasonicated until clear, then transferred to a 50 mL stainless steel autoclave for solvothermal reaction at 398 K for 6 h. After cooling the autoclave to room temperature, the solids were collected by centrifugation (8000 rpm) and washed several times with DMF and ethanol (EtOH). Afterwards, the product was dried in vacuum at 333 K for 12 h to obtain a pale pink MIL-68(In/Fe).

2.3. Synthesis of MIL-68(In/Fe) sulfurized In_2S_3/Fe_3S_4 (M-ISFS)

First of all, 100 mg of prepared MIL-68(In/Fe) and 400 mg of thioacetamide (TAA) were dispersed in 10 mL ethanol and labelled A and B respectively. Two of them were stirred for 10 min. Following the ultrasonic dispersion of A for 30 min, it was mixed with completely dissolved B. Then the mixture was transferred to a 50 mL stainless steel autoclave for solvothermal reaction at 393 K for 8 h. After cooling the autoclave to room temperature, the solids were collected by centrifugation (8000 rpm) and washed several times with ultrapure water and EtOH. Afterwards, the product was dried in vacuum at 333 K for 12 h to obtain a brown M-ISFS.

2.4. Synthesis of other catalysts

MIL-68(In) sulfurized In_2S_3 (M-IS), MIL-68(Fe) sulfurized Fe_3S_4 (M-FS) and one-pot synthesized Fe_3S_4/In_2S_3 were synthesized for simultaneously investigation. Detailed information of synthesis can be found in Text S2.

2.5. Characterization of catalysts

Detailed information on the characterizations applied was presented in Text S3.

2.6. ATZ photo-Fenton degradation process

Before the experiments, the digital optical power and energy meter were used to measure the actual intensity received at different reaction sites (Fig. S1). The average intensity value is 26.79 $mW \cdot cm^{-2}$, which is close to the intensity in a cloudy day [32]. The degradation performances of the as-prepared catalysts were evaluated in a multi-position photochemical reactor (HF-GHX-VII, Shanghai Hefan Co., China) using a simulated sunlight by a 300 W xenon lamp equipped with circulating water to guarantee the room temperature. For a typical degradation process, catalyst (0.15 $g \cdot L^{-1}$) was dispersed in 50 mL of ATZ solution (15 $mg \cdot L^{-1}$) and transferred into a quartz test tube with magnetic stirring in darkness for 30 min to counterpoise the adsorption-desorption. Then, H_2O_2 (4 mM) was added at the same time to open the xenon lamp. During the degradation process, 1.0 mL of solution was collected with a syringe at 10 min intervals and filtered via a 0.22 μm nylon membrane to get rid of the catalyst. For reusability experiments, M-ISFS was separated by centrifugation after experiment, washed with ethanol and dried for next using. For real water sample, the initial pH was adjusted from the original 7.8–8.0 to 5.3–5.7 after simple filtration.

2.7. Analytical methodology

The concentration (C) of ATZ was analyzed using a HPLC (Waters, USA) with 2998 photo-diode array (PDA) ultraviolet detector and a ZORBAX SB C18 (4.6×250 mm, 5 μm) column. The degradation efficiency (η) was calculated according to Eq. (1), while the kinetic rates of ATZ degradation were calculated according to Eq. (2) via the pseudo-first-order model. C_0 and C are the initial concentrations and concentrations at the sampling time t (min) of ATZ ($mg \cdot L^{-1}$) respectively, and k is the kinetic rate constant (min^{-1}).

$$\eta\ (\%) = \frac{(C_0 - C)}{C_0} \times 100\% \tag{1}$$

$$ln\left(\frac{C_0}{C}\right) = kt \tag{2}$$

Acetonitrile and water (65:35, v/v) was used as the mobile phase with a flow rate of 1.0 $mL \cdot min^{-1}$. Inductively Coupled Plasma Mass Spectrometry (ICP-MS, Thermo Fisher iCAP TQ, USA) was used for analyzing the concentration of metal ions in the degradation. The concentration of ATZ was determined at 222 nm. Electron spin resonance (ESR, Bruker EMX plus, Germany) spectra were recorded for analysis of the radical produced during the photo-Fenton degradation. MS (Agilent 6400 Series Quadrupole, USA) was applied to analyze the intermediates and degradation path of ATZ. The toxicities of ATZ and its intermediates were estimated using ecological structure activity relationship prediction software (ECOSAR 2.2).

3. Results and discussion

3.1. Characterization

The morphological changes between MIL-68(In/Fe) and M-ISFS were investigated by SEM characterization. MIL-68(In/Fe) showed well-crystallized pencil-like structures with an average length of approximately 3 μm (Fig. 1a), which is differed significantly from the irregular rod structures of MIL-68(Fe) and hexagonal micro-rods structures of MIL-68(In) [33,34]. After sulfurization, the obtained M-ISFS (Fig. 1b) exhibited an amorphous shape consisting of an accumulation of larger smooth square pieces and small pieces. Considering the piece-like structure that may be formed during the synthesis of In_2S_3 [35] and the possibility of MOF collapse due to long-time sulfurization [24], it can be postulated that the small fragments may have originated directly from MIL-68(In/Fe) that fragmentated during the sulfurization process, while the larger square-shaped pieces are formed through the further growth of In_2S_3 in the sulfide. The EDS elemental mappings of M-ISFS were illustrated in Fig. 1c-f, showing uniform distribution of the elements In, Fe, and S. The TEM images of M-ISFS were shown in Fig. S2. It can be observed the clear contact interface between In_2S_3 and Fe_3S_4, providing a channel for the transport of photogenerated carriers. Mapping images exhibited that Fe was mainly distributed on small pieces, whereas In was more prevalent on the smooth large square pieces. The presence of Fe, In, and S in M-ISFS was further confirmed through the energy dispersive spectroscopy (EDS) (Fig. S3). Additionally, the EDS analysis (Table S1) revealed that the relative atomic content of elements S, Fe, and In were 50.62 %, 35.42 %, and 13.96 % respectively, aligning closely with the expected values based on the synthesis process.

The XRD patterns of MIL-68(In/Fe), M-FS, M-IS and M-ISFS were shown in Fig. 1g. MIL-68(In/Fe) exhibited distinct diffraction peaks at 2θ = 8.3°, 9.6°, 14.3°, 16.5° and 19.1°, confirming that MIL-68(In/Fe) exhibited a crystalline structure. Three diffraction peaks of M-FS situated at 2θ = 15.5°, 25.4° and 30.0° were in alignment with the (111), (220) and (311) crystal planes of Fe_3S_4 (JCPDS 16–0713). The broad diffraction peaks of M-IS revealed at 2θ = 27.6°, 32.7° and 48.2°,

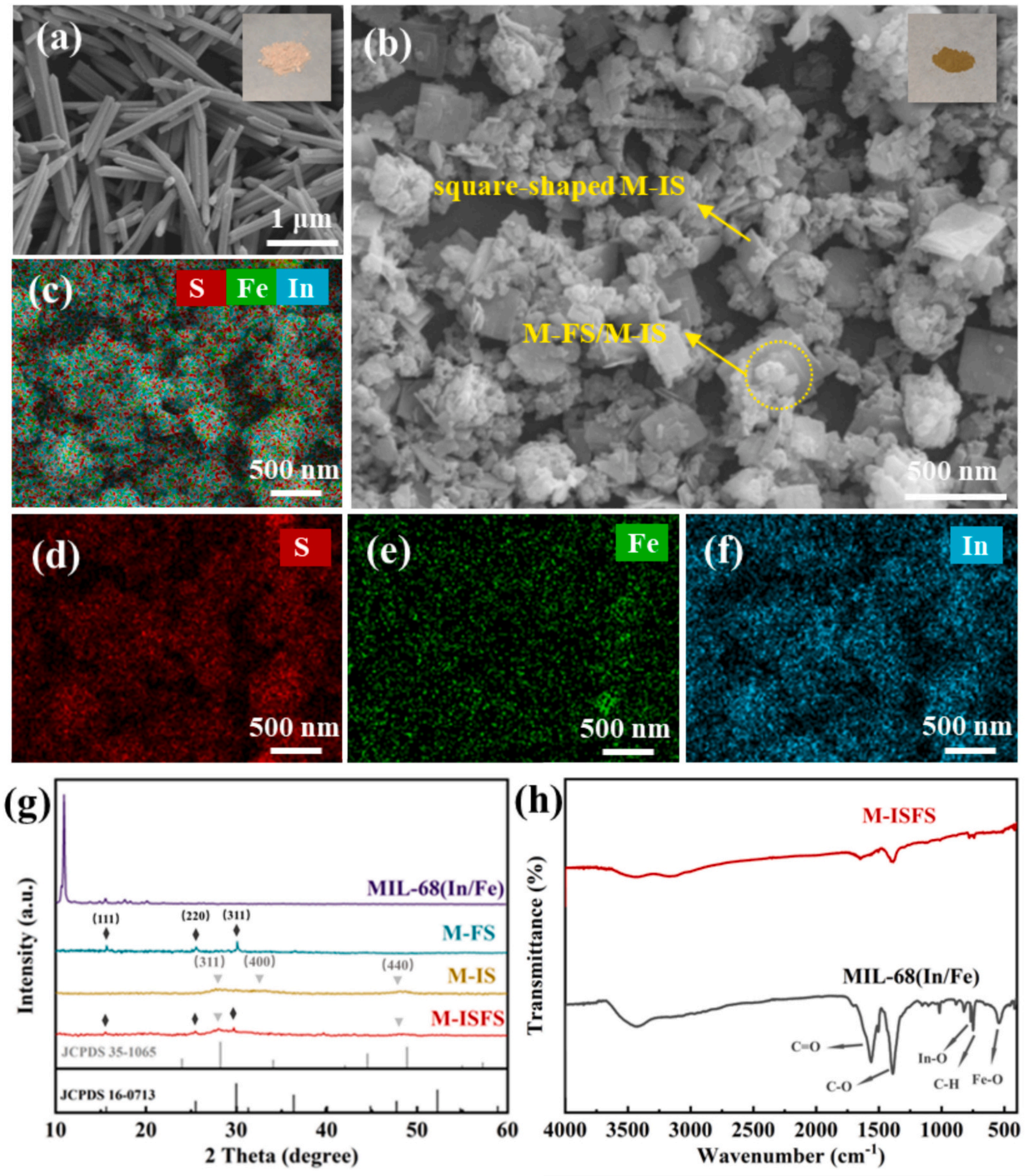

Fig. 1. SEM images of (a) MIL-68(In/Fe) and (b) M-ISFS; (c-f) EDS elemental mapping images of M-ISFS; (g) XRD patterns of MIL-68(In/Fe), M-FS, M-IS and M-ISFS; (h) FT-IR patterns of M-ISFS and MIL-68(In/Fe).

corresponding to the (311), (400) and (440) crystal planes, which is consistent with the reported β-In_2S_3 [36]. Additionally, diffraction peaks of M-ISFS were found at 2θ = 15.5°, 25.4°, 27.6°, 30.0° and 48.2°, indicating the presence of M-FS and M-IS in M-ISFS. It was noteworthy that despite a relatively low Fe content in M-ISFS, the pattern of M-ISFS still exhibited distinct diffraction peaks corresponding to M-FS. In addition, the peaks of M-ISFS were not completely consistent with the expected angles of $FeIn_2S_4$ shown in the JCPDS 35–1065, indicating that M-ISFS was not a bimetallic sulfide but a composite of two monometallic sulfides.

The formation of M-ISFS was further confirmed by the Fourier transform infrared spectrum (FT-IR) (Fig. 1h). Absorbances at 1560 cm^{-1}, 1388 cm^{-1} and 746 cm^{-1} of MIL-68(In/Fe) were attributed to stretching vibrations of C═O, C—O and C—H bonds, respectively [37]. Peaks at 579 cm^{-1} and 786 cm^{-1} may correspond to the Fe—O and In—O bonds [38,39]. However, the absorption peaks of organic bonds in M-ISFS were largely absent, suggesting that MIL-68 was almost transformed into M-ISFS upon treatment with TAA. In addition, the chemical bonding of MIL-68(In/Fe) showed distinct characteristic peaks in Raman spectra (Fig. S4). After TAA treatment, the intensity of these characteristic peaks is markedly reduced, demonstrating a transformation from MIL-68(In/Fe) to M-ISFS.

The elemental compositions and surface electronic states of as prepared catalysts were characterized via XPS. The survey elemental mapping (Fig. 2a) indicated that M-ISFS was mainly composed of In, Fe and S, which was consistent with the results of EDS mapping (Fig. 1c-f). The characteristic peaks of M-ISFS at 444.7 eV and 452.4 eV in Fig. 2b corresponded to the orbitals In $3d_{3/2}$ and In $3d_{5/2}$. With respect to the M-IS, the binding energies of these orbitals were negatively shifted by 0.2 eV and 0.2 eV, respectively. The peaks of M-ISFS at 711.7 eV and 725.3 eV in Fig. 2c corresponded to the orbitals Fe $2p_{3/2}$ and Fe $2p_{1/2}$. With respect to the M-FS, the binding energies of these orbitals were positively shifted by 0.5 eV and 0.6 eV, respectively. The peaks of M-ISFS in Fig. 2d located at 161.5 eV and 162.6 eV, which were attributed to the orbitals S $2p_{3/2}$ and S $2p_{1/2}$. The binding energies of these orbitals were also found to be positively shifted with respect to the M-FS, but negatively shifted with respect to the M-IS. The loss of electrons from the elements in a substance can result in a positive shift of the corresponding characteristic peaks, and vice versa [40]. Consequently, the presence of significant interactions and electron transfer activity within M-ISFS may likely due to the formation of heterostructures.

The surface area and pore distribution of MIL-68(In/Fe) and M-ISFS were explored via nitrogen adsorption-desorption isotherms experiments (Fig. S5). The surface areas of MIL-68(In/Fe) and M-ISFS were 41.881 $m^2 \cdot g^{-1}$ and 70.913 $m^2 \cdot g^{-1}$, respectively. M-ISFS obtained by sulfurization exhibited a greater specific surface area than the precursor MOF. The total pore volume of M-ISFS were 0.352 $cm^3 \cdot g^{-1}$, which was markedly increased compared to MIL-68(In/Fe) (0.134 $cm^3 \cdot g^{-1}$). An increased surface area and pore volume facilitate interactions between catalysts and ATZ, which may positively influence catalytic performance [41,42].

3.2. Optical and electronic analysis

The optical response properties of M-FS, M-IS and M-ISFS were investigated by ultraviolet-visible diffused reflectance spectroscopy (UV–vis DRS) (Fig. 3a). The absorption band of M-IS was mainly in the wavelength range of 200–500 nm, while M-FS exhibited significant absorption of both the ultraviolet and visible light (200–800 nm). The absorption edge of M-ISFS was red-shifted relative to M-IS, indicating that it can be excited by sunlight. The band gaps of M-FS, M-IS and M-ISFS were calculated via Kubelka-Munk function:

$$\alpha h\nu = A\left(h\nu - E_g\right)^{n/2} \tag{3}$$

where h, α, ν, A, and E_g is the Planck constant, absorption coefficient,

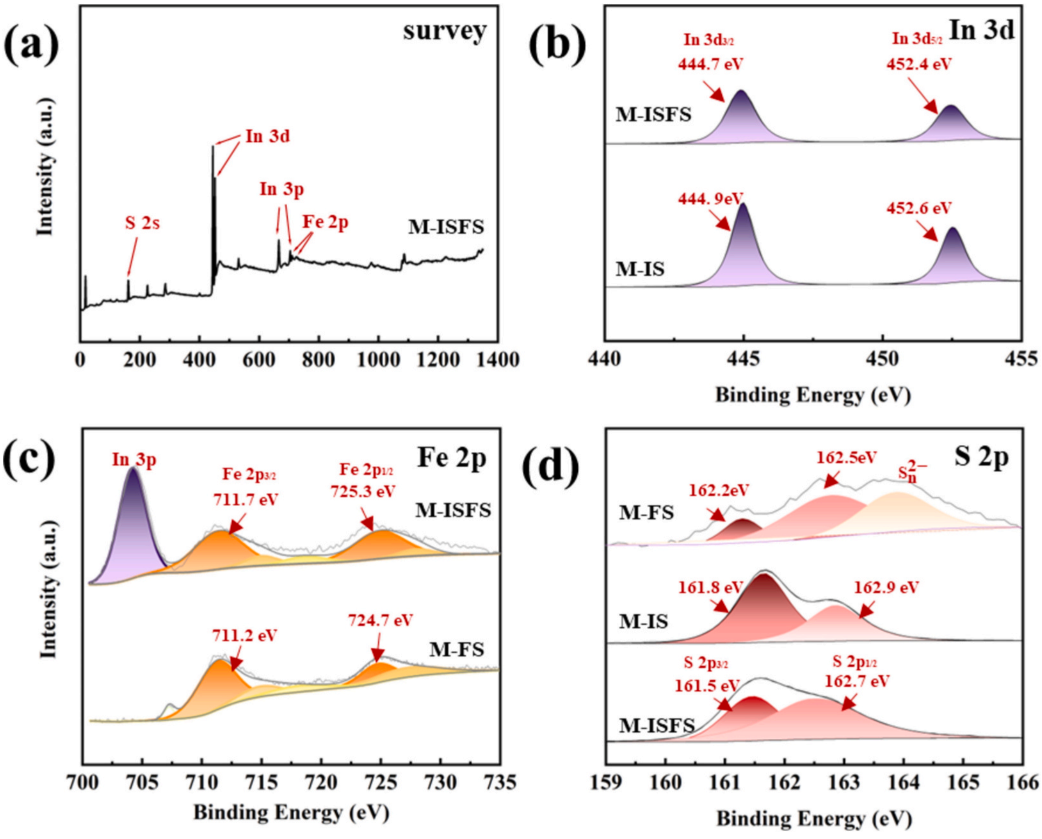

Fig. 2. XPS spectra of M-ISFS, M-IS and M-FS: (a) survey, (b) In 3d, (c) Fe 2p and (d) S 2p.

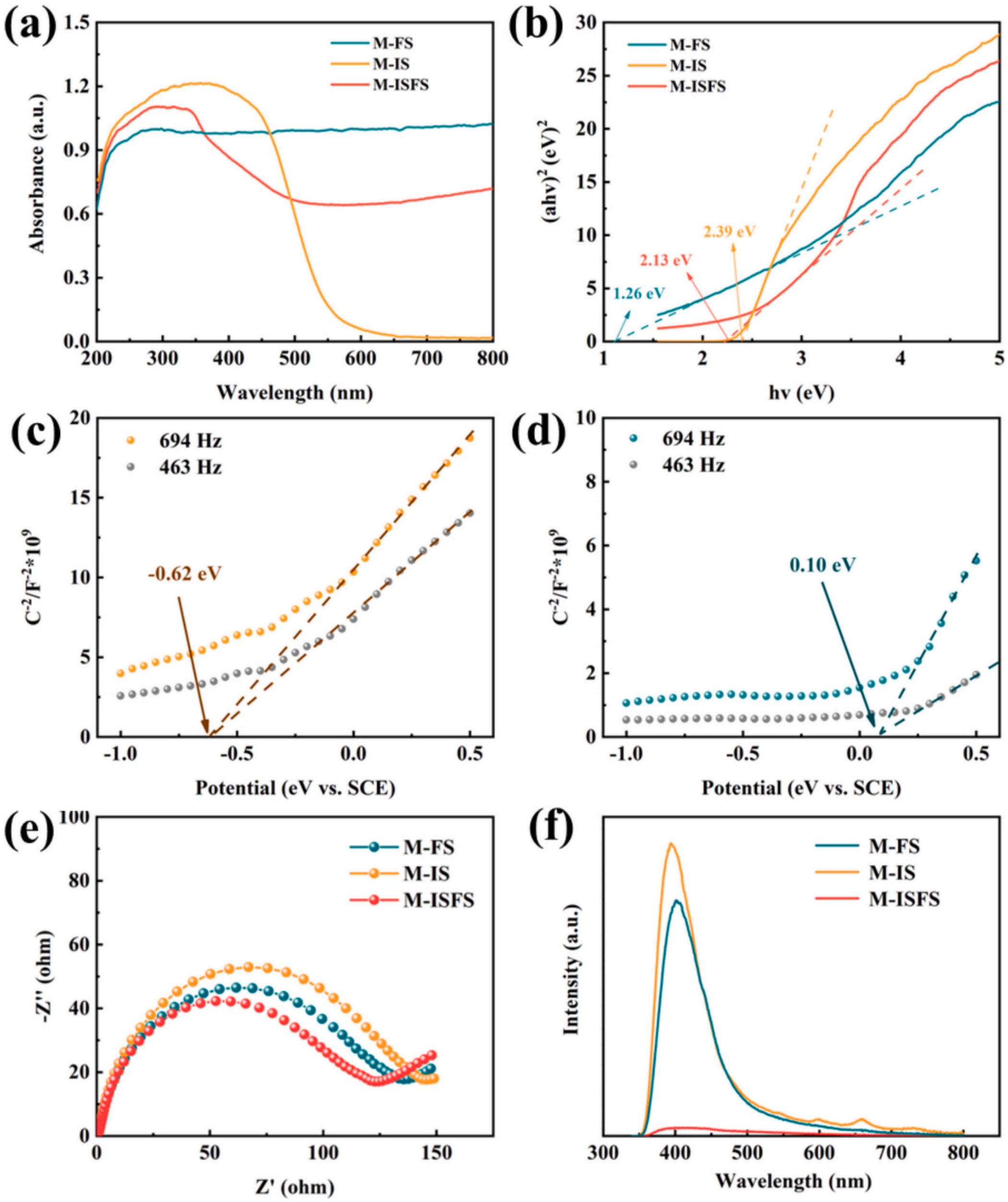

Fig. 3. (a) UV–vis diffuse reflectance spectra and (b) Tauc plots of as prepared catalysts; Mott-Schottky curves of (c) M-IS and (d) M-FS; (e) EIS and (f) PL curves of M-IS, M-FS and M-ISFS.

light frequency, a constant, and the band gap energy, respectively. The E_g of M-FS, M-IS and M-ISFS were 1.26 eV, 2.39 eV and 2.13 eV respectively (Fig. 3b). It was apparent that the E_g of M-ISFS was diminished as a consequence of the combination of M-FS and M-IS.

Mott-Schottky (MS) tests of M-FS and M-IS were conducted for further investigation of conduction band potential (E_{CB}) and valence band potential (E_{VB}) (Fig. 3c-d). The MS curves for M-FS and M-IS both exhibited positive slopes, indicating n-type semiconductor characteristic [43]. According to the curve intercepts, the flat band potentials of M-FS and M-IS were approximately 0.10 eV vs. SCE and −0.62 eV vs. SCE respectively. Typically, the E_{CB} of n-type semiconductors is approximately 0.2 eV higher than the flat band potential [44]. Following the conversion and adjustment of the aforementioned results, the E_{CB} of M-FS and M-IS should be 0.14 eV vs. NHE and −0.58 eV vs. NHE, respectively. On the basis of the formula Eq. (4), the E_{VB} of M-FS and M-IS are 1.40 eV vs. NHE and 1.81 eV vs. NHE respectively.

$$E_{VB} = E_{CB} + E_g \tag{4}$$

Due to the E_{CB} of M-IS is more negative than that of M-FS, there is a possibility of electron transfer from M-IS to M-FS. Besides, the transient photocurrent response test (Fig. S6) showed the response of M-ISFS was notably stronger than that of M-FS and M-IS, implying more efficient photo-generated electron transfer and higher photo-generated electron-hole separation efficiency. The smaller the semicircular radius of the catalyst in the EIS test, the less its charge transfer resistance of the corresponding catalyst. As shown in **Fig. 3**e, M-ISFS had the smallest radius compared to M-IS and M-FS, indicating that M-ISFS had the best charge transfer capability and photogenerated electrons could be quickly transferred to the solid iron center to facilitate Fe^{3+}/Fe^{2+} cycling. The PL intensities of catalysts represent the recombination extent of photo-generated carriers. As displayed in Fig. 3f, the intensity of M-ISFS is the weakest than the M-IS and M-FS, confirming the lowest recombination of photogenerated carriers.

3.3. Photo-Fenton activity of M-ISFS

The photo-Fenton performance of M-IS, M-FS, MIL-68(In/Fe), and Fe_3S_4/In_2S_3 were presented in Fig. 4a. The degradation rates of ATZ by M-IS and MIL-68(In/Fe) were only 9.9 % and 22.5 %, respectively. In contrast, M-FS exhibited a degradation rate of 86.5 %, potentially attributed to the Fenton reaction and the exposure of catalytic sites [45]. M-ISFS demonstrated superior photo-Fenton performance by degrading 99.6 % of the ATZ, which may be attributed to the formation of heterostructures. In addition, M-ISFS also exhibited a higher degradation capacity compared to one-pot synthesized Fe_3S_4/In_2S_3 (85.9 %). Compared with M-FS ($k = 0.0333$ min^{-1}), M-ISFS with lower Fe content also exhibited a higher kinetic rate constant ($k = 0.0905$ min^{-1}), which is approximately 2.72 times that of M-FS (Fig. 4b).

The degradation efficiency of ATZ in different systems was compared in Fig. 4c. The adsorption capacity of M-ISFS was evaluated without irradiation. The consistent adsorption removal rate of ATZ was about 0.9 %, indicating the influence of adsorption can be ignored. H_2O_2 alone was ineffective in degrading ATZ, but exposure to simulated sunlight resulted in a degradation rate of 33.9 %. This may be due to the generation of ·OH by H_2O_2 in the presence of light [46]. Without adding H_2O_2, only 4.9 % of ATZ was degraded by M-ISFS under irradiation. The M-ISFS + H_2O_2 system exhibited enhanced degradation efficacy in comparison to previously examined systems, achieving degradation rates of up to 61.2 %. However, the incorporation of simulated sunlight in the M-ISFS + H_2O_2 system significantly increased the degradation efficiency, reaching 99.6 %, surpassing the degradation rates observed in other systems. The kinetic rate constant of the M-ISFS + H_2O_2 + light system ($k = 0.0905$ min^{-1}) was notably higher than that of any other system, and even 6.16 times that of the dark Fenton reaction ($k = 0.0147$ min^{-1}) (Fig. 4d). It is apparent that the sum of M-ISFS, H_2O_2, and light act separately in the system cannot reach this rate, and therefore synergistic effects exist. Determination of H_2O_2 consumption was conducted for both the photo and dark Fenton process (Fig. S7). Concentration of H_2O_2 was 2.6 mM in the light Fenton system by the end of degradation, which was less than 3.2 mM in the dark Fenton system, suggesting that the photo-Fenton system was more efficient in utilizing hydrogen H_2O_2. Due to the shielding effect of KSCN on Fe sites in the Fenton reaction [47], we analyzed the contribution of Fe sites to photo-Fenton degradation by KSCN masking experiments (Fig. S8). The Fe sites were almost completely masked when the dose of KSCN reached 1.0 $g·L^{-1}$. Simultaneously, the degradation rate sharply decreased from the original 99.6 % to 14.6 %, which indicated that the Fe sites played a dominant role in the photo-Fenton reaction.

The influence of different ATZ concentrations from 5 to 25 $mg·L^{-1}$ on photo-Fenton process was shown in Fig. 5a. M-ISFS showed significant degradation at all five concentrations of ATZ. Among them, it was able to degrade 90.0 % of ATZ even at 25 $mg·L^{-1}$. The influence of different initial H_2O_2 concentrations from 2 to 10 mM was presented in Fig. 5b. An initial concentration of 4 mM H_2O_2 was found to be optimal for M-ISFS in degrading 15 $mg·L^{-1}$ of ATZ. However, an increase in the initial concentration of H_2O_2 to 10 mM led to a significant decrease in degradation efficiency. This may be attributed to the excessive H_2O_2 may react with ·OH to produce the less oxidizing $·HO_2$ [48]. The influence of different M-ISFS dosages from 0.05 to 0.25 $g·L^{-1}$ was illustrated in Fig. 5c. It was observed that the degradation rate of ATZ gradually enhanced with increasing initial dosage, peaking at 0.15 $g·L^{-1}$. A slight decrease was be observed upon increasing the initial dosage to 0.25 $g·L^{-1}$, possibly due to the over-dosing catalyst which increased turbidity and impeded light energy utilization.

The effects of different pH values from 3 to 8 on degradation were shown in Fig. 5d. The efficiency of ATZ degradation gradually increased

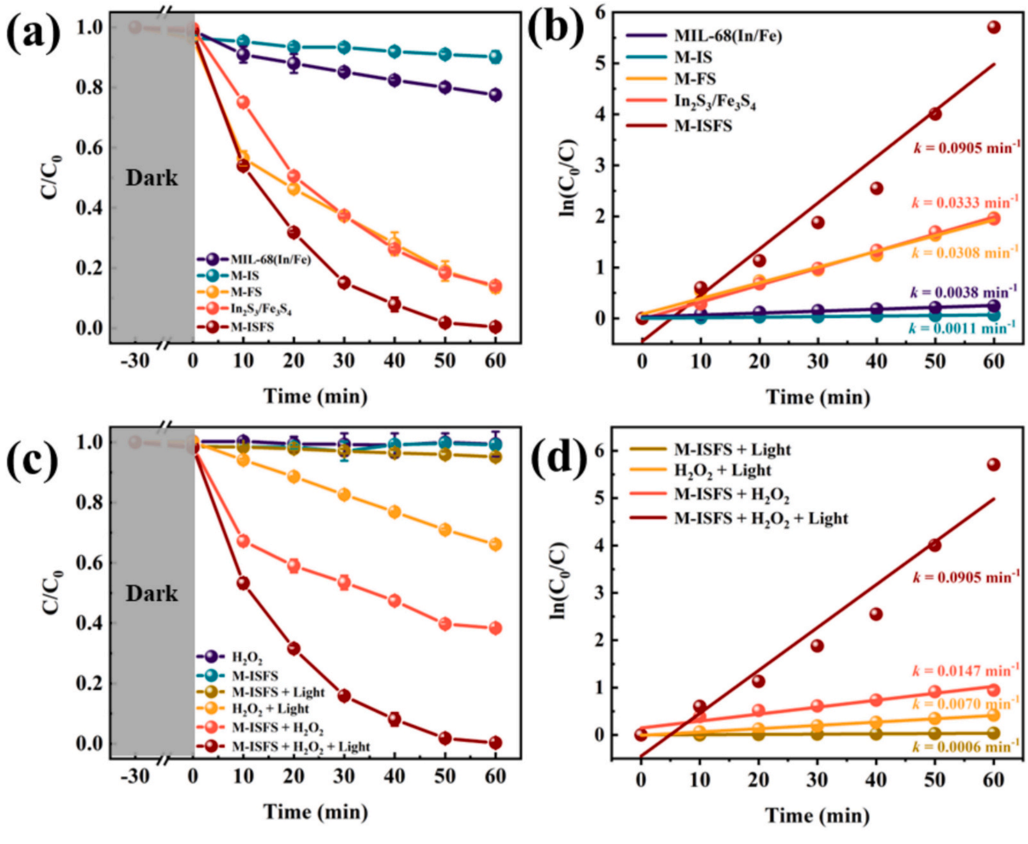

Fig. 4. ATZ degradation efficiencies (a) and plots of $\ln(C_0/C)$ versus time (b) over different catalysts; ATZ degradation efficiencies (c) and plots of $\ln(C_0/C)$ versus time (d) in different systems. Reaction conditions: M-ISFS dosage = 0.15 $g·L^{-1}$, ATZ concentration = 15 $mg·L^{-1}$, initial H_2O_2 concentration = 4 mM, initial pH = 5.3–5.7 (unadjusted). The error bars derived from three replicate experiments.

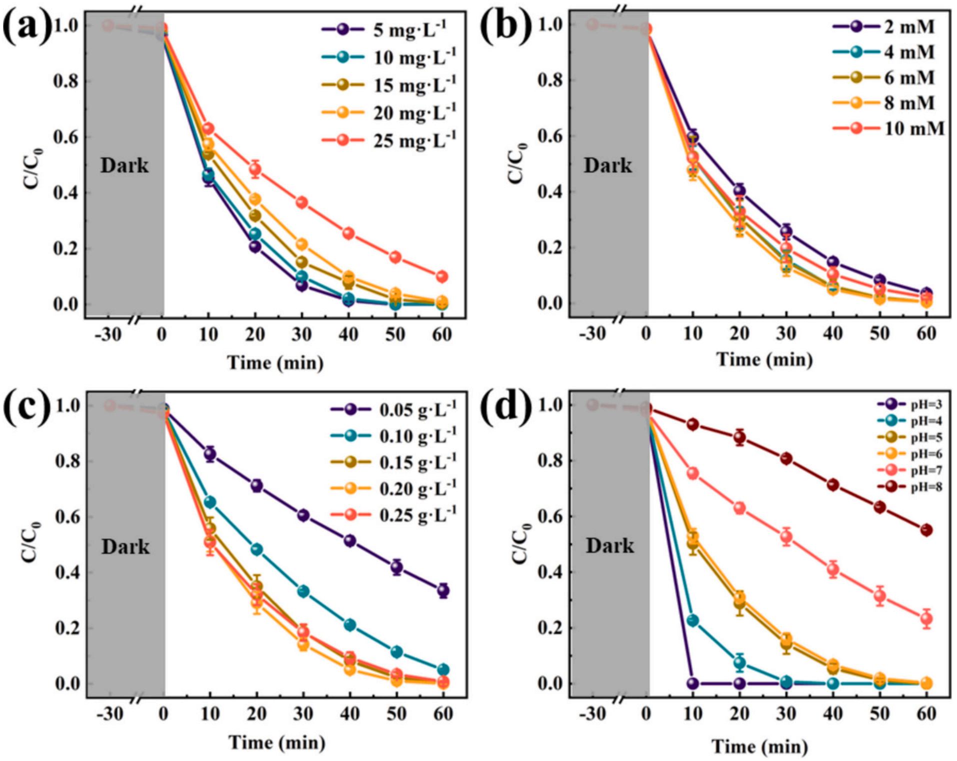

Fig. 5. Photo-Fenton degradation efficiencies of ATZ over different (a) ATZ concentrations, (b) initial H_2O_2 concentrations, (c) M-ISFS dosages and (d) initial pH values. Reaction conditions: M-ISFS dosage = 0.15 $g \cdot L^{-1}$ (for a, b and d), ATZ concentration = 15 $mg \cdot L^{-1}$ (for b, c and d), initial H_2O_2 concentration = 4 mM (for a, c and d), initial pH = 5.3–5.7 (unadjusted). The error bars derived from three replicate experiments.

with the decrease of pH, and it was completely degraded within 10 and 30 min at pH 3 and 4, respectively. At pH 5 or 6, the degradation of ATZ remained consistently above 99 %. However, with increasing pH, the catalytic efficiency of M-ISFS gradually decreased, resulting in degradation rates of 76.7 % and 44.9 % at pH 7 and 8, respectively. It was possible that the elevated pH levels may result in the ineffective decomposition of H_2O_2, consequently diminishing the production of reactive species [49]. Following the systematic consideration of the degradation efficiency and associated consumption of catalyst, the conditions (M-ISFS dosage = 0.15 $g \cdot L^{-1}$, ATZ concentration = 15 $mg \cdot L^{-1}$, initial H_2O_2 concentration = 4 mM, initial pH unadjusted) were selected for subsequent experiments.

The interference of eight common ions on the photo-Fenton degradation process was illustrated in Fig. 6a-b. In the presence of HCO_3^-, the photo-Fenton process was significantly impeded, with only 4.9 % of ATZ being degraded. This may be attributed to the consumption of ·OH in the conversion of HCO_3^- to CO_3^{2-} and the shielding effect of CO_3^{2-} on Fe^{2+} sites [50]. However, it was reassuring that four cations and three other anions did not inhibit the degradation. For universality investigation, several typical contaminants were selected, including the antibiotic ciprofloxacin (CIP), the fungicide carbendazim (CBZ), and the insecticide imidacloprid (IMI) (Fig. 6e). The M-ISFS demonstrated to degrade all three contaminants with 100 % efficiency within a brief period. In particular, CIP was degraded completely in less than 20 min. The reusability of M-ISFS was depicted in Fig. 6f. The degradation rates were 99.6 %, 98.8 %, 96.5 % and 88.7 % from the first to the fourth use. In the first three uses, M-ISFS exhibited a high degradation rate and the degradation efficiency remained almost unchanged (99.6 %, 98.8 %, 96.5 %). On the fourth use, the degradation efficiency slightly decreased to 88.7 %, which may be due to oxidation of the catalyst surface [51].

In order to assess the degradation performance of M-ISFS in a real setting, experiments were conducted using water samples from Taihu Lake near the farmland aggregation area. The precise location was illustrated in Fig. 6c. The degradation rate of spiked ATZ reached 64.2 % after 60 min of light exposure (Fig. 6d). Based on the results of the anion interference experiment, the most likely culprit for the decrease in degradation is HCO_3^- in water. In addition, humic acids (HA) that may be present in the water can shield the catalytic sites [52], resulting in low yields of reactive species. Therefore, the effect of humic acid on degradation was also explored and exhibited in Fig. S9. Following the addition of HA, the degradation rate of ATZ was decreased to 47 %, indicating the inhibitory effect of HA on photo-Fenton degradation. Metal ion concentrations were measured in the photo-Fenton process and the results were provided in Fig. S10. Apparently, the concentrations of both In and Fe ions increased after the photo-Fenton process.

M-ISFS was compared with the currently reported photo-Fenton catalysts regarding the degradation of ATZ (Table S2). M-ISFS exhibits superior degradation capabilities (99.6 % in 60 min) compared to most catalysts in the photo-Fenton system. It is noteworthy that the initial dosage requirement of M-ISFS for ATZ is the lowest and that M-ISFS also exhibits a relatively low initial H_2O_2 concentration requirement. Comparing to other MOF-derived catalysts for photo-Fenton-degradation, M-ISFS also possessed better performance.

3.4. *Photo-Fenton degradation mechanism*

To ascertain the influence of diverse reactive species in the photo-Fenton degradation of ATZ by M-ISFS, a series of trapping experiments was undertaken by introduction of different scavengers. Isopropyl alcohol (IPA), 1,4-benzoquinone (p-BQ), ethylenediaminetetraacetic acid disodium salt (EDTA-2Na), furfuryl alcohol (FFA) and N_2 were applied for trapping ·OH, $\cdot O_2^-$, h^+, $^1O_2$ and O_2 [53,54], respectively. In Fig. 7a, the presence of scavengers leaded to a decrease in the catalytic performance of M-ISFS, indicating that all these reactive species contributed to the degradation process. Among them, degradation was most significantly inhibited when $^1O_2$ and ·OH were captured. In

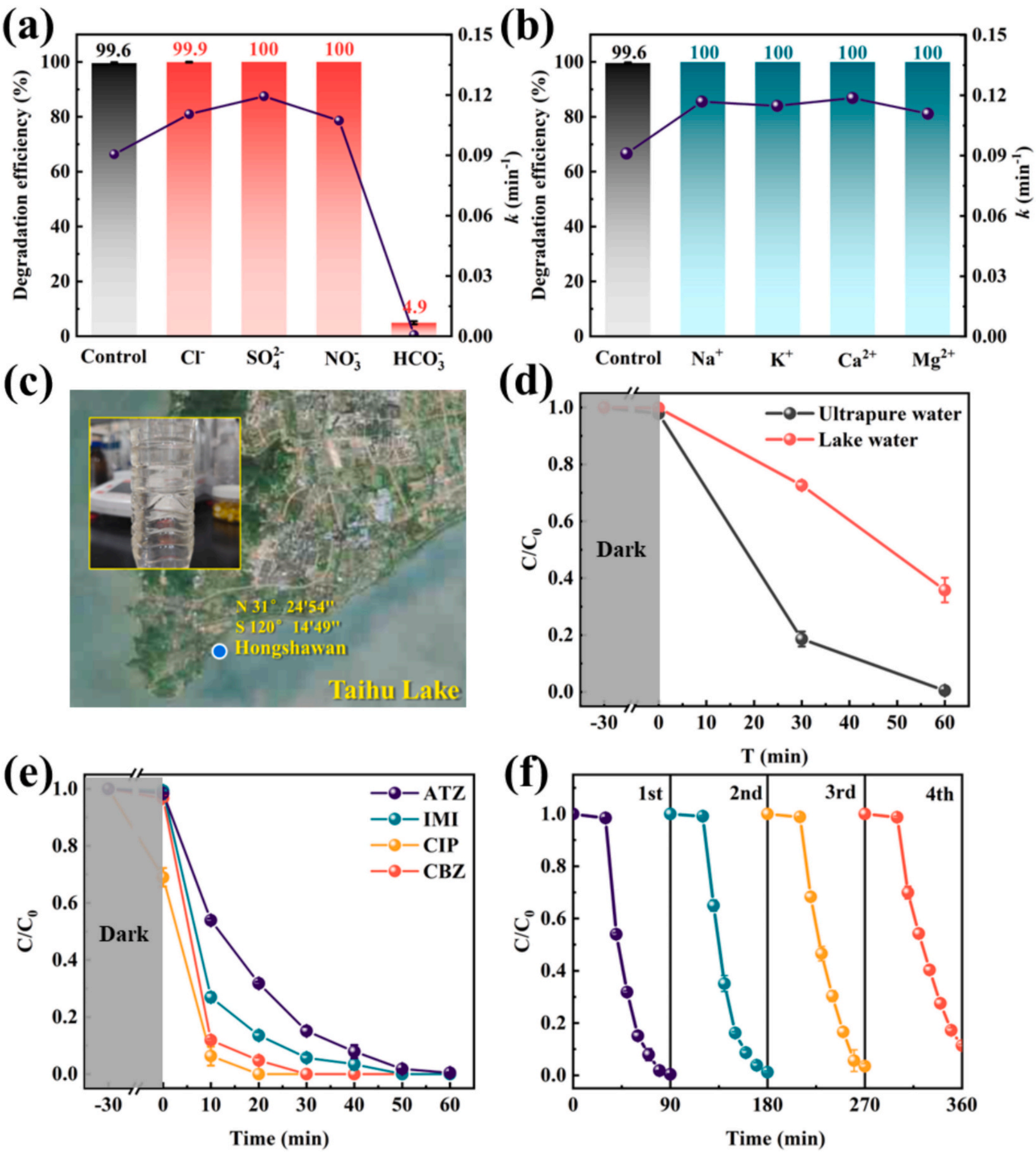

Fig. 6. (a-b) Photo-Fenton degradation efficiencies of M-ISFS with different ions (ion concentration = 1 mM); (c) sampling location of the real water; Photo-Fenton degradation efficiencies of M-ISFS (d) in real water sample, (e) on different contaminations and (f) of the different number of applications. Reaction conditions: M-ISFS dosage = 0.15 $g\cdot L^{-1}$, contaminant concentration = 15 $mg\cdot L^{-1}$, initial H_2O_2 concentration = 4 mM, initial pH = 5.3–5.7 (unadjusted). The error bars derived from three replicate experiments.

addition, the degradation rate of ATZ was significantly decreased under N_2 atmosphere, indicating the contribution of O_2 in photo-Fenton process.

To further identify the types of active species involved in degradation, the ESR spin-trap technology was adopted to investigate the presence of reactive species in the reaction system. In Fig. 7b, the characteristic quadruple peak of ·OH was significantly observed under both irradiation and dark, which confirmed the important role of ·OH. However, the increase after irradiation in response intensity was not significant, suggesting that ·OH was not the main reason for the significant increase in degradation efficiency under irradiation. As demonstrated in Fig. 7c, the response of $^1O_2$ was weak in dark, but significantly promoted under irradiation. Simultaneously, the increase in the response of $^1O_2$ under light was the highest of the three response species measured, indicating that light may facilitate the multichannel production of $^1O_2$ [55,56]. In Fig. 7d, the response intensity of $\cdot O_2^-$ was the lowest that of the three reactive species, which was consistent with the results of previous experiments. However, the response intensity of $\cdot O_2^-$ also increased significantly under irradiation. Although ·OH, $\cdot O_2^-$ and $^1O_2$ are the main reactive species involved in the photo-Fenton reaction, the promotion of the degradation efficiency under irradiation is primarily attributed to the high production of $^1O_2$ and $\cdot O_2^-$.

The proposed photo-Fenton reaction mechanism of M-ISFS was presented in Fig. 8. Firstly, the reaction between H_2O_2 and Fe^{3+} on the surface of M-ISFS resulted in the generation of ·OH, with Fe^{2+} subsequently being oxidized to Fe^{3+}(Eq. (5)). Upon irradiation, carrier separation occurred on M-ISFS, leading to the generation of e^- and h^+(Eq. (6)). The heterogeneous structure of M-ISFS allowed for the transfer of e^- from the conduction band of M-IS to the conduction band of M-FS (Eq. (7)). Subsequent reduction by e^-(Eq. (8)) enabled Fe^{2+} to continue participating in the decomposition of H_2O_2. Furthermore, H_2O_2 might also be converted into ·OH via acquiring e^-(Eq. (9)). Then, the generated ·OH and O_2 could be converted to $\cdot O_2^-$(Eq. (10−12) [57]. However, the conduction band potential of M-FS did not reach the redox potential of $O^2/\cdot O_2^-$ (−0.33 eV) [58], the reaction (Eq. (12)) would only occur on the M-IS. Additionally, $\cdot O_2^-$ and ·OH can be converted to $^1O_2$ through

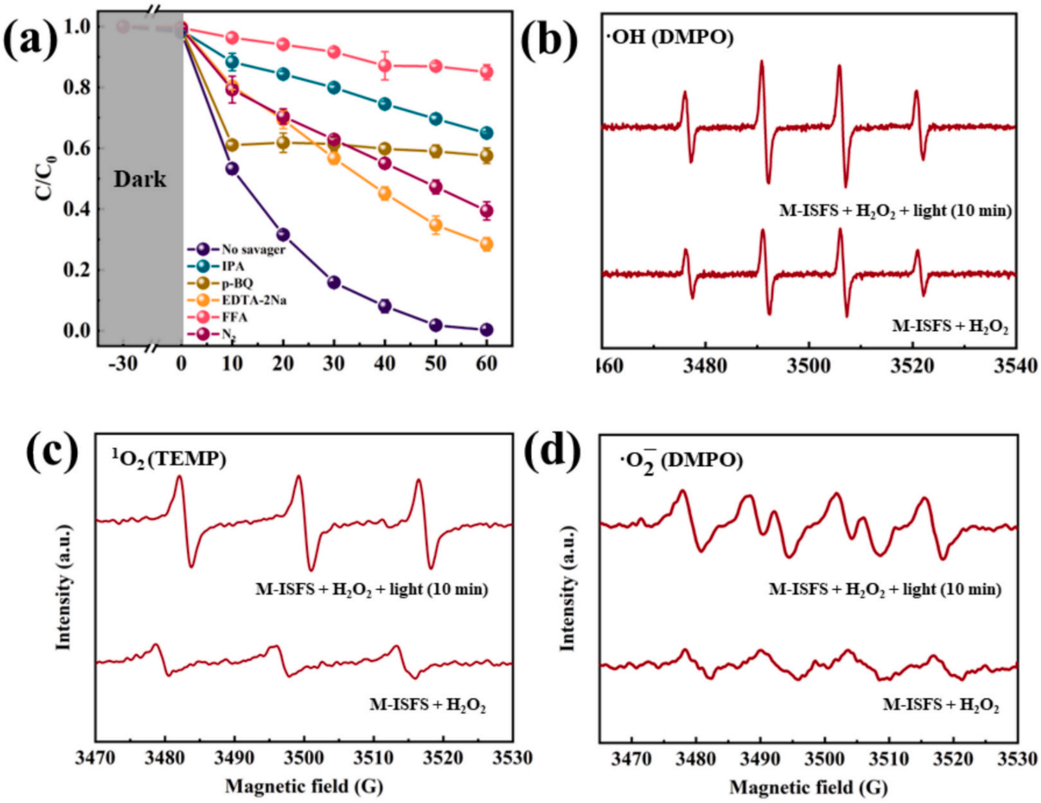

Fig. 7. (a) The effects of different scavengers on photo-Fenton degradation efficiency; ESR spectra of (b) DMPO-·OH, (c) TEMP-^{1}O. and (d) DMPO-·O_2^-. Reaction conditions: M-ISFS dosage = 0.15 $g \cdot L^{-1}$, contaminant concentration = 15 $mg \cdot L^{-1}$, initial H_2O_2 concentration = 4 mM, initial pH = 5.3–5.7 (unadjusted). The error bars derived from three replicate experiments.

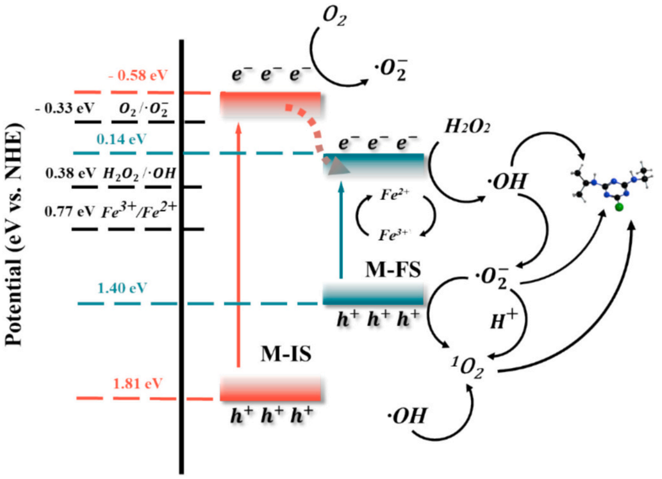

Fig. 8. Photo-Fenton degradation mechanism of M-ISFS.

multiple pathways (Eq. (13–16) [59]. Notably, the consumption of e^- resulted in the efficient separation of h^+, leading to the accelerated generation of $^1O_2$. Eventually, ATZ was degraded under the attack of various reactive species.

$$Fe^{2+} + H_2O_2 \rightarrow Fe^{3+} + \cdot OH + OH^- \tag{5}$$

$$M - ISFS + hv \rightarrow h_{VB}^+ + e_{CB}^- \tag{6}$$

$$e_{CB}^- \ (M - IS) \rightarrow e_{CB}^- \ (M - FS) \tag{7}$$

$$Fe^{3+} + e_{CB}^- \ (M - FS) \rightarrow Fe^{2+} \tag{8}$$

$$H_2O_2 + e_{CB}^- \rightarrow \cdot OH \tag{9}$$

$$\cdot OH + H_2O_2 \rightarrow \cdot O_2^- + H_2O + H^+ \tag{10}$$

$$2H_2O_2 \rightarrow 2H_2O + O_2 \tag{11}$$

$$O_2 + e_{CB}^- \ (M - IS) \rightarrow \cdot O_2^- \tag{12}$$

$$\cdot O_2^- + \cdot OH \rightarrow {}^1O_2 + OH^- \tag{13}$$

$$2 \cdot O_2^- + 2H^+ \rightarrow {}^1O_2 + H_2O_2 \tag{14}$$

$$\cdot O_2^- + h_{VB}^+ \rightarrow {}^1O_2 \tag{15}$$

$$4 \cdot OH \rightarrow {}^1O_2 + 2H_2O \tag{16}$$

3.5. Degradation products and toxicity assessment

To elucidate the degradation pathways of ATZ during the photo-Fenton reaction and the formation of intermediates, density functional theory (DFT) calculations were performed on ATZ molecule. Fig. 9a illustrated the electrostatic potential spectra (ESP) of ATZ, with red and blue indicating the negative electrostatic and positive electrostatic regions, respectively. These two regions are prone to reduction and oxidation reactions, respectively. The lowest unoccupied molecular orbital (LUMO) and highest occupied molecular orbital (HOMO) of ATZ molecule were shown in Fig. 9b-c, which clearly indicated the electron-poor and electron-rich sites. The Fukui function was calculated for specifying the nucleophilic (f^+), electrophilic (f^-) and free radical (f^0) active sites in molecules, with higher values indicating greater possibility to suffer corresponding attack [60]. Additionally, condensed dual descriptors (CDD) can be used for determining the specific reaction

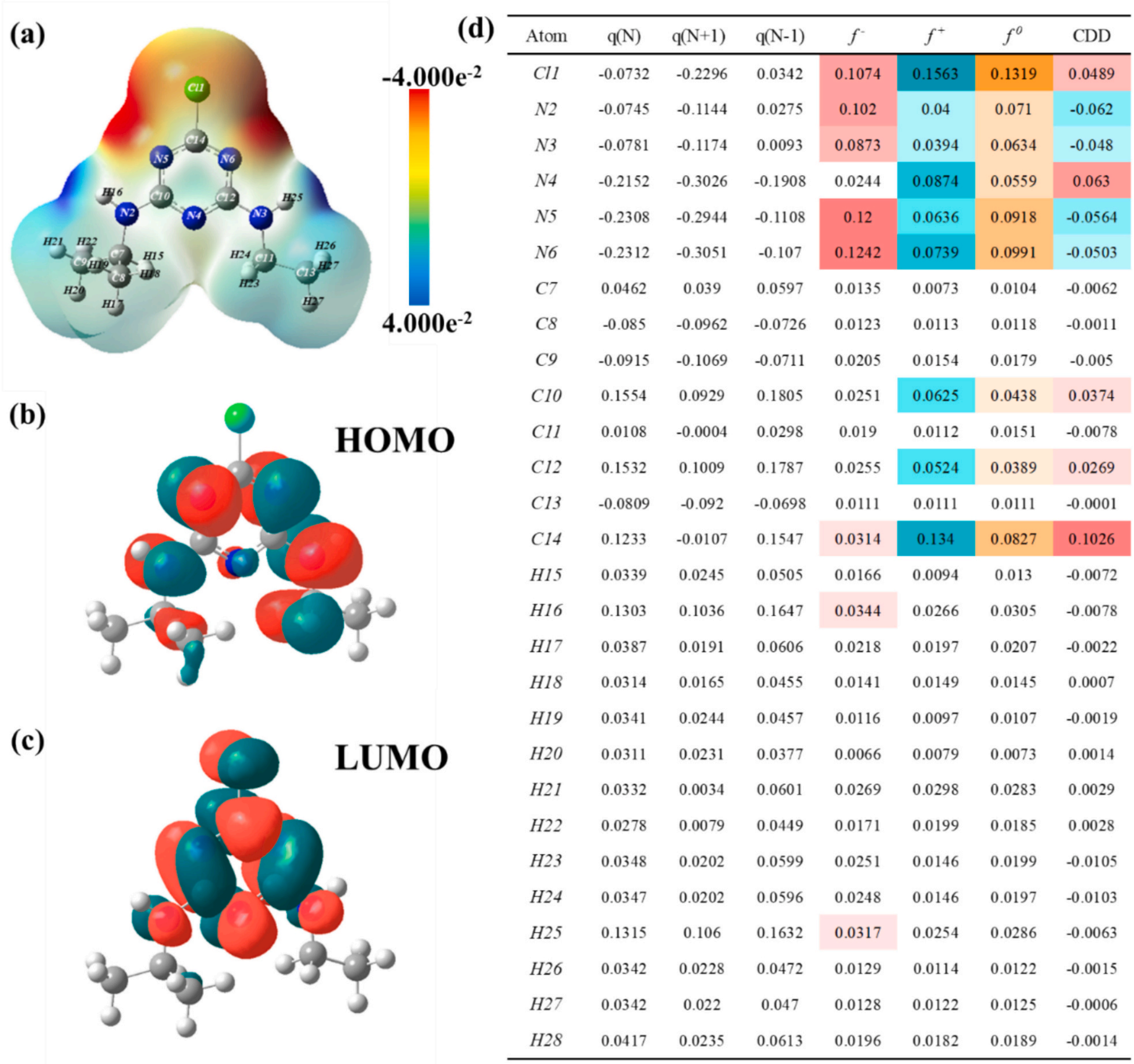

Atom	q(N)	q(N+1)	q(N-1)	f^-	f^+	f^0	CDD
Cl1	-0.0732	-0.2296	0.0342	0.1074	0.1563	0.1319	0.0489
N2	-0.0745	-0.1144	0.0275	0.102	0.04	0.071	-0.062
N3	-0.0781	-0.1174	0.0093	0.0873	0.0394	0.0634	-0.048
N4	-0.2152	-0.3026	-0.1908	0.0244	0.0874	0.0559	0.063
N5	-0.2308	-0.2944	-0.1108	0.12	0.0636	0.0918	-0.0564
N6	-0.2312	-0.3051	-0.107	0.1242	0.0739	0.0991	-0.0503
C7	0.0462	0.039	0.0597	0.0135	0.0073	0.0104	-0.0062
C8	-0.085	-0.0962	-0.0726	0.0123	0.0113	0.0118	-0.0011
C9	-0.0915	-0.1069	-0.0711	0.0205	0.0154	0.0179	-0.005
C10	0.1554	0.0929	0.1805	0.0251	0.0625	0.0438	0.0374
C11	0.0108	-0.0004	0.0298	0.019	0.0112	0.0151	-0.0078
C12	0.1532	0.1009	0.1787	0.0255	0.0524	0.0389	0.0269
C13	-0.0809	-0.092	-0.0698	0.0111	0.0111	0.0111	-0.0001
C14	0.1233	-0.0107	0.1547	0.0314	0.134	0.0827	0.1026
H15	0.0339	0.0245	0.0505	0.0166	0.0094	0.013	-0.0072
H16	0.1303	0.1036	0.1647	0.0344	0.0266	0.0305	-0.0078
H17	0.0387	0.0191	0.0606	0.0218	0.0197	0.0207	-0.0022
H18	0.0314	0.0165	0.0455	0.0141	0.0149	0.0145	0.0007
H19	0.0341	0.0244	0.0457	0.0116	0.0097	0.0107	-0.0019
H20	0.0311	0.0231	0.0377	0.0066	0.0079	0.0073	0.0014
H21	0.0332	0.0034	0.0601	0.0269	0.0298	0.0283	0.0029
H22	0.0278	0.0079	0.0449	0.0171	0.0199	0.0185	0.0028
H23	0.0348	0.0202	0.0599	0.0251	0.0146	0.0199	-0.0105
H24	0.0347	0.0202	0.0596	0.0248	0.0146	0.0197	-0.0103
H25	0.1315	0.106	0.1632	0.0317	0.0254	0.0286	-0.0063
H26	0.0342	0.0228	0.0472	0.0129	0.0114	0.0122	-0.0015
H27	0.0342	0.022	0.047	0.0128	0.0122	0.0125	-0.0006
H28	0.0417	0.0235	0.0613	0.0196	0.0182	0.0189	-0.0014

Fig. 9. (a) ESP mapping, (b) HOMO orbital, (c) LUMO orbital and (d) the Fukai index of ATZ molecule.

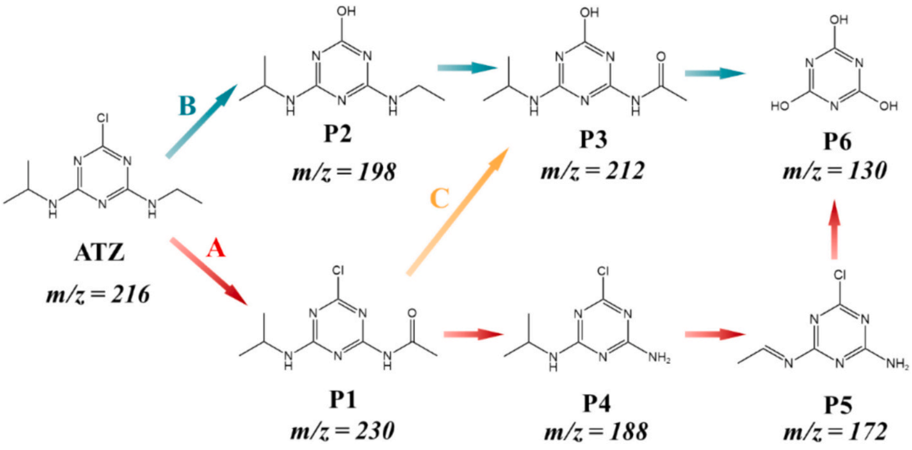

Fig. 10. Photo-Fenton degradation pathways of ATZ.

orientation of atoms when the electrophilicity and nucleophilicity are equivalent [61]. According to the results in Fig. 9d, the *Cl1*, *N2*, *N3*, *N5* and *N6* are identified as the most vulnerable sites for attack. Among them, *Cl1* is vulnerable to be substituted by OH group due to its relatively high f^0 and f^+ value, while *N2*, *N3*, *N5* and *N6* are vulnerable to be attacked by $^1O_2$ due to their relatively high f^- value. However, due to the high steric hindrance and saturated bonds, these atoms are difficult to be attacked by $^1O_2$ [62,63]. Thus, based on the distribution of HOMO on the lateral chain in Fig. 9b, *C8*, *C11* and *Cl1* are most possible to be attack.

Combining the analysis above and the degradation intermediates obtained from MS (Fig. S11), the degradation pathways were proposed in Fig. 10. For pathway A, the ethylamine group on the ATZ molecule was attacked by $^1O_2$, resulting in the formation of compound P1. Subsequently P1 was deamidated to form P4. P4 transformed to P5 after olefination of the isopropylamine group, while P5 was converted to P6 after dealkylation, dechlorination and hydroxylation. For pathway B, ATZ was attacked by ·OH, leading to dechlorination and hydroxylation, ultimately yielding P2. Subsequent oxidation of P2 resulted in the formation of P3, which was further transformed into P6 via dealkylation and hydroxylation. In addition, P1 may also suffer a ·OH attack to transform into P3. Finally, P6 underwent a ring-off reaction to form products with simpler structures.

ECOSAR was adopted in predictive assessments of acute and chronic toxicity towards aquatic organisms by contaminations. Based on the analyzed intermediates, the predictions regarding both acute and chronic toxicity on fish, daphnid and green algae were classified in Table S3–4 and exhibited in Fig. S12**.** The toxicities of intermediates P4 and P5 are relatively high for all three aquatic organisms, particularly for daphnid. However, the overall toxicities of P6 are found to be significantly diminished. Apparently, the environmental risk of ATZ can be significantly reduced after undergoing a M-ISFS-mediated photo-Fenton degradation.

4. Conclusion

In this paper, heterostructured M-ISFS sulfurized from MIL-68(In/Fe) was synthesized and successfully employed in the weak sunlight photo-Fenton degradation of ATZ. The M-ISFS possessed ample Fe sites, excellent light absorption capacities, and preferable carrier separation properties. It achieved a 99.6 % degradation of ATZ within 60 min using a low initial catalyst dosage and weak sunlight intensity and the degradation rate constant of which was approximately 2.72 times that of M-FS. It also exhibited satisfactory recyclability and universality. The main reactive species analyzed in the degradation process were $^1O_2$, ·OH and $\cdot O_2^-$. DFT indicated that *C8*, *C11* and *Cl1* in the ATZ molecule may be the initial targets of attack, in accordance with the results obtained by MS. The investigation of the degradation pathway and toxicities revealed that the toxicities of ATZ can be markedly diminished following M-ISFS-mediated sunlight photo-Fenton degradation. The prepared heterostructured M-ISFS sulfurized from bimetallic MOF are promising for the high efficiency photo-Fenton degradation.

CRediT authorship contribution statement

Hong-Ming Zhang: Writing – original draft, Methodology, Investigation, Formal analysis, Data curation. **Shu-Ting Cheng:** Methodology, Data curation, Conceptualization. **Xiao-Fang Shen:** Project administration, Methodology, Funding acquisition. **Yue-Hong Pang:** Writing – review & editing, Supervision, Project administration, Funding acquisition.

Declaration of competing interest

The authors declare that they have no known competing financial interests or personal relationships that could have appeared to influence the work reported in this paper.

Acknowledgments

This work was supported by the National Natural Science Foundation of China (22276077, 22076067).

Appendix A. Supplementary data

Supplementary data to this article can be found online at https://doi.org/10.1016/j.jwpe.2024.106520.

Data availability

Data will be made available on request.

References

[1] U.S. Geological Survey, National Water-Quality Assessment (NAWQA) Project. https://water.usgs.gov/nawqa/pnsp/usage/maps/show_map.php?year=2019&map=ATRAZINE&hilo=L&disp=Atrazine/, 2019 (accessed 15 April 2024).
[2] C. Chevrier, G. Limon, C. Monfort, F. Rouget, R. Garlantezec, C. Petit, G. Durand, S. Cordier, Urinary biomarkers of prenatal atrazine exposure and adverse birth outcomes in the PELAGIE birth cohort, Environ. Health Perspect. 119 (2011) 1034–1041.
[3] M. Dehghani, E. Gharehchahi, S. Jafari, Z. Moeini, Z. Derakhshan, M. Ferrante, G. O. Conti, Health risk assessment of exposure to atrazine in the soil of shiraz farmlands, Iran, Environ. Res. 204 (2022) 112090.
[4] T.B. Hayes, V. Khoury, A. Narayan, M. Nazir, A. Park, T. Brown, L. Adame, E. Chan, D. Buchholz, T. Stueve, S. Gallipeau, Atrazine induces complete feminization and chemical castration in male African clawed frogs (Xenopus laevis), Proc. Natl. Acad. Sci. USA 107 (2010) 4612–4617.
[5] Q. Zhou, L. Chen, Z. Wang, J. Wang, S. Ni, J. Qiu, X. Liu, X. Zhang, X. Chen, Fast atrazine degradation by the mixed cultures enriched from activated sludge and analysis of their microbial community succession, Environ. Sci. Pollut. Res. Int. 24 (2017) 22152–22157.
[6] M. Beaulieu, H. Cabana, Z. Taranu, Y. Huot, Predicting atrazine concentrations in waterbodies across the contiguous United States: the importance of land use, hydrology, and water physicochemistry, Limnol. Oceanogr. 65 (2020) 2966–2983.
[7] J.M. Montiel Leon, S. Vo Duy, G. Munoz, M.F. Bouchard, M. Amyot, S. Sauve, Quality survey and spatiotemporal variations of atrazine and desethylatrazine in drinking water in Quebec, Canada, Sci. Total Environ. 671 (2019) 578–585.
[8] H. Almasi, A. Takdastan, N. Jaafarzadeh, A.A. Babaei, Y. Tahmasebi Birgani, B. Cheraghian, A. Saki, S. Jorfi, Spatial distribution, ecological and health risk assessment and source identification of atrazine in Shadegan international wetland, Iran, Mar. Pollut. Bull. 160 (2020) 111569.
[9] L. Zhang, Y. Huang, H. Yan, Y. Cheng, Y.X. Ye, F. Zhu, G. Ouyang, Oxygen-centered organic radicals-involved unified heterogeneous self-Fenton process for stable mineralization of micropollutants in water, Adv. Mater. 29 (2024) 2401162.
[10] A.N. Soon, B.H. Hameed, Heterogeneous catalytic treatment of synthetic dyes in aqueous media using Fenton and photo-assisted Fenton process, Desalination 269 (2011) 1–16.
[11] F. Li, P. Wang, M. Li, T. Zhang, Y. Li, S. Zhan, Efficient photo-Fenton reaction for tetracycline and antibiotic resistant bacteria removal using hollow Fe-doped In_2O_3 nanotubes: from theoretical research to practical application, Water Res. 240 (2023) 120088.
[12] M. Perez-Moya, M. Graells, G. Castells, J. Amigo, E. Ortega, G. Buhigas, L.M. Perez, H.D. Mansilla, Characterization of the degradation performance of the sulfamethazine antibiotic by photo-Fenton process, Water Res. 44 (2010) 2533–2540.
[13] M. Cheng, Y. Liu, D. Huang, C. Lai, G. Zeng, J. Huang, Z. Liu, C. Zhang, C. Zhou, L. Qin, W. Xiong, H. Yi, Y. Yang, Prussian blue analogue derived magnetic cu-Fe oxide as a recyclable photo-Fenton catalyst for the efficient removal of sulfamethazine at near neutral pH values, Chem. Eng. J. 362 (2019) 865–876.
[14] A.M. Díez, M.M. Moreira, M. Pazos, M.A. Sanromán, T. Albergaria, C. Delerue-Matos, Pesticide abatement using environmentally friendly nano zero valent particles as photo-Fenton catalyst, Sep. Purif. Technol. 336 (2024) 126179.
[15] K. Sun, H. Yuan, Y. Yan, H. Qin, L. Sun, L. Tan, F. Guo, X. Du, W. Shi, Visible-light-response 2D/2D $Bi_2Fe_4O_9/ZnIn_2S_4$ van der Waals S-scheme heterojunction with efficient photocatalysis-self-Fenton degradation of antibiotics, J. Water Process Eng. 58 (2024) 104803.
[16] E. Coronado, G., Minguez Espallargas, dynamic magnetic MOFs, Chem. Soc. Rev. 42 (2013) 1525–1539.
[17] Z. Wang, Y. Cheng, C. Wang, R. Guo, J. You, H. Zhang, Optimizing the performance of Fe-based metal-organic frameworks in photo-Fenton processes: mechanisms, strategies and prospects, Chemosphere 339 (2023) 139673.
[18] Q. Wang, Q. Gao, A.M. Al Enizi, A. Nafady, S. Ma, Recent advances in MOF-based photocatalysis: environmental remediation under visible light, Inorg. Chem. Front. 7 (2020) 300–339.

[19] A. Dhakshinamoorthy, Z. Li, S. Yang, H. Garcia, Metal-organic framework heterojunctions for photocatalysis, Chem. Soc. Rev. 53 (2024) 3002–3035.

[20] Y. Zhang, J. Xu, J. Zhou, L. Wang, Metal-organic framework-derived multifunctional photocatalysts, Chinese, J. Catal. 43 (2022) 971–1000.

[21] W. Ji, Z. Xu, P. Liu, S. Zhang, W. Zhou, H. Li, T. Zhang, L. Li, X. Lu, J. Wu, W. Zhang, F. Huo, Metal-organic framework derivatives for improving the catalytic activity of the CO oxidation reaction, ACS Appl. Mater. Interfaces 9 (2017) 15394–15398.

[22] T. Bao, Y. Xia, J. Lu, C. Zhang, J. Wang, L. Yuan, Y. Zhang, C. Liu, C. Yu, A Pacman-like titanium-doped cobalt sulfide hollow superstructure for Electrocatalytic oxygen evolution, Small 18 (2022) 2103106.

[23] H. Zhu, S. Dong, J. Xiong, P. Wan, X. Jin, S. Lu, Y. Zhang, H. Fan, MOF derived cobalt-nickel bimetallic phosphide (CoNiP) modified separator to enhance the polysulfide adsorption-catalysis for superior lithium-sulfur batteries, J. Colloid Interface Sci. 641 (2023) 942–949.

[24] T. De Villenoisy, X. Zheng, V. Wong, S.S. Mofarah, H. Arandiyan, Y. Yamauchi, P. Koshy, C.C. Sorrell, Principles of design and synthesis of metal derivatives from MOFs, Adv. Mater. 35 (2023) 2210166.

[25] H. Zhang, Z. Wang, J. Zhang, K. Dai, Metal-sulfide-based heterojunction photocatalysts: principles, impact, applications, and in-situ characterization, Chinese, J. Catal. 49 (2023) 42–67.

[26] Z. Liu, F. Jin, X. Li, P. Zhang, Z. Jin, Morphological effects of WO_3 in metal sulfide-based S-scheme heterojunctions for boosting photocatalytic hydrogen production, J. Mater. Sci. Technol. 188 (2024) 131–143.

[27] Y. Hu, M. Nie, P. Hong, J. He, Y. Li, K. Zhang, D. Yang, L. Jiang, J. Liu, L. Kong, Defect-engineered WO_3-x@MoS_2 hollow tube exhibiting enhanced Fenton-like and photocatalytic activities via electric field rearrangement and band alignment, Appl. Catal. B Environ. 320 (2023) 122013.

[28] P. Zhu, Y. Wang, P. Ma, S. Li, F. Fan, K. Cui, S. Ge, Y. Zhang, J. Yu, Low-power and high-performance trimethylamine gas sensor based on n-n heterojunction microbelts of Perylene Diimide/CdS, Anal. Chem. 91 (2019) 5591–5598.

[29] W. Gao, W. Liu, Y. Leng, X. Wang, X. Wang, B. Hu, D. Yu, Y. Sang, H. Liu, In2S3 nanomaterial as a broadband spectrum photocatalyst to display significant activity, Appl. Catal. B Environ. 176-177 (2015) 83–90.

[30] Z. He, M.S. Siddique, H. Yang, Y. Xia, J. Su, B. Tang, L. Wang, L. Kang, Z. Huang, Novel Z-scheme In_2S_3/Bi_2WO_6 core-shell heterojunctions with synergistic enhanced photocatalytic degradation of tetracycline hydrochloride, J. Clean. Prod. 339 (2022) 130634.

[31] J. Wei, Q. Wang, M. He, S. Li, Y. Zhang, Y. Yang, S. Luo, L. Fu, X. Wang, T. Yang, Construction of Fe(III) doping modified AgI/NH_2-MIL-68(in/Fe) Z-scheme heterojunction photocatalysts through unique internal and interfacial charge transmission and separation efficiency, Appl. Surf. Sci. 612 (2023) 155726.

[32] Y. Zhang, C. Tong, L. Shi, Y. Yin, S. Lou, J. Liu, S. Liao, L. Liu, D. Zhang, Polyurethane sponge assisted recoverable photocatalyst for outdoor weak sunlight-driven efficient water purification, Appl. Surf. Sci. 638 (2023) 158091.

[33] Y. Jin, F. Liu, Y. Li, Q. Du, F. Song, B. Chen, K. Chen, Y. Zhang, M. Wang, Y. Sun, S. Zhao, Z. Jing, X. Pi, Y. Wang, D. Wang, Efficient adsorption of azo anionic dye Congo red by micro-nano metal-organic framework MIL-68(Fe) and MIL-68(Fe)/chitosan composite sponge: preparation, characterization and adsorption performance, Int. J. Biol. Macromol. 252 (2023) 126198.

[34] Y. Pi, S. Jin, X. Li, S. Tu, Z. Li, J. Xiao, Encapsulated MWCNT@MOF-derived In_2S_3 tubular heterostructures for boosted visible-light-driven degradation of tetracycline, Appl. Catal. B Environ. 256 (2019) 117882.

[35] L. Wang, B. Zhao, C. Wang, M. Sun, Y. Yu, B. Zhang, Thermally assisted photocatalytic conversion of CO_2-H_2O to C2H4over carbon doped In2S3nanosheets, J. Mater. Chem. A 8 (2020) 10175–10179.

[36] J. Singh, R.K. Soni, J. Kim, Photocatalytic β-In_2S_3 nanoflowers synthesized by thermal assembly of In_2S_3 nanosheets, J. Alloys Compd. 911 (2022) 165099.

[37] D. Xie, Y. Ma, Y. Gu, H. Zhou, H. Zhang, G. Wang, Y. Zhang, H. Zhao, Bifunctional NH_2-MIL-88(Fe) metal–organic framework nanooctahedra for highly sensitive detection and efficient removal of arsenate in aqueous media, J. Mater. Chem. A 5 (2017) 23794–23804.

[38] F. Zhao, Y. Liu, S.B. Hammouda, B. Doshi, N. Guijarro, X. Min, C.-J. Tang, M. Sillanpää, K. Sivula, S. Wang, MIL-101(Fe)/g-C_3N_4 for enhanced visible-light-driven photocatalysis toward simultaneous reduction of Cr(VI) and oxidation of bisphenol a in aqueous media, Appl. Catal. B Environ. 272 (2020) 119033.

[39] H.E. Emam, R.M. Abdelhameed, Anti-UV radiation textiles designed by embracing with Nano-MIL (Ti, in)-metal organic framework, ACS Appl. Mater. Interfaces 9 (2017) 28034–28045.

[40] J. Bao, X. Jiang, L. Huang, W. Quan, C. Zhang, Y. Wang, H. Wang, Y. Zeng, W. Zhang, Y. Ma, S. Yu, X. Hu, H. Tian, Molybdenum disulfide loading on a Z-scheme graphitic carbon nitride and lanthanum nickelate heterojunction for enhanced photocatalysis: interfacial charge transfer and mechanistic insights, J. Colloid Interface Sci. 611 (2022) 684–694.

[41] H. Yi, C. Lai, X. Huo, L. Qin, Y. Fu, S. Liu, L. Li, M. Zhang, M. Chen, G. Zeng, H_2O_2-free photo-Fenton system for antibiotics degradation in water via the synergism of oxygen-enriched graphitic carbon nitride polymer and nano manganese ferrite, Environ. Sci-Nano 9 (2022) 815–826.

[42] H. Yi, D. Ma, X. Huo, L. Li, M. Zhang, X. Zhou, F. Xu, H. Yan, G. Zeng, C. Lai, Facile introduction of coordinative Fe into oxygen-enriched graphite carbon nitride for efficient photo-Fenton degradation of tetracycline, J. Colloid Interface Sci. 660 (2024) 692–702.

[43] X. Wu, N. Kang, X. Li, Z. Xu, S.A.C. Carabineiro, K. Lv, 2D/2D layered $BiOIO_3$/g-C_3N_4 S-scheme heterojunction for photocatalytic NO oxidation, J. Mater. Sci. Technol. 196 (2024) 40–49.

[44] Z. He, Y. Xia, J. Su, B. Tang, Fabrication of magnetically separable $NiFe_2O_4/Bi_{24}O_{31}Br_{10}$ nanocomposites and excellent photocatalytic performance under visible light irradiation, Opt. Mater. 88 (2019) 195–203.

[45] J. Hang, X.H. Yi, C.C. Wang, H. Fu, P. Wang, Y. Zhao, Heterogeneous photo-Fenton degradation toward sulfonamide matrix over magnetic Fe_3S_4 derived from MIL-100 (Fe), J. Hazard. Mater. 424 (2022) 127415.

[46] Q.M. Chen, C. Yang, N.K. Goh, K.C. Teo, B. Chen, Photochemical degradation of 1,3-dinitrobenzene in aqueous solution in the presence of hydrogen peroxide, Chemosphere 55 (2004) 339–344.

[47] F. Xu, C. Lai, M. Zhang, D. Ma, L. Li, S. Liu, X. Zhou, H. Yan, N. Wang, M. Xu, L. Qin, H. Yi, Graphite carbon nitride coupled with high-dispersed iron (II) phthalocyanine for efficient oxytetracycline degradation under photo-Fenton process: performance and mechanism, Sep. Purif. Technol. 308 (2023) 122829.

[48] Y. Jia, C. Wu, D.H. Kim, B.W. Lee, S.J. Rhee, Y.C. Park, C.S. Kim, Q.J. Wang, C. Liu, Nitrogen doped $BiFeO_3$ with enhanced magnetic properties and photo-Fenton catalytic activity for degradation of bisphenol a under visible light, Chem. Eng. J. 337 (2018) 709–721.

[49] W. Fu, J. Yi, M. Cheng, Y. Liu, G. Zhang, L. Li, L. Du, B. Li, G. Wang, X. Yang, When bimetallic oxides and their complexes meet Fenton-like process, J. Hazard. Mater. 424 (2022) 127419.

[50] C. Zhao, J. Wang, X. Chen, Z. Wang, H. Ji, L. Chen, W. Liu, C.C. Wang, Bifunctional $Bi_{12}O_{17}Cl_2$/MIL-100(Fe) composites toward photocatalytic Cr(VI) sequestration and activation of persulfate for bisphenol a degradation, Sci. Total Environ. 752 (2021) 141901.

[51] Y. Shi, X. Wang, X. Liu, C. Ling, W. Shen, L. Zhang, Visible light promoted Fe_3S_4 Fenton oxidation of atrazine, Appl. Catal. B Environ. 277 (2020) 119229.

[52] J. Zhang, D. Wang, F. Zhao, J. Feng, H. Feng, J. Luo, W. Tang, Ferrate modified carbon felt as excellent heterogeneous electro-Fenton cathode for chloramphenicol degradation, Water Res. 227 (2022) 119324.

[53] F. Xu, C. Lai, M. Zhang, B. Li, L. Li, S. Liu, D. Ma, X. Zhou, H. Yan, X. Huo, B. Wang, H. Yi, L. Qin, L. Tang, High-loaded single-atom cu-N_3 sites catalyze hydrogen peroxide decomposition to selectively induce singlet oxygen production for wastewater purification, Appl. Catal. B Environ. 339 (2023) 123075.

[54] F. Xu, C. Lai, M. Zhang, B. Li, S. Liu, M. Chen, L. Li, Y. Xu, L. Qin, Y. Fu, X. Liu, H. Yi, X. Yang, Facile one-pot synthesis of carbon self-doped graphitic carbon nitride loaded with ultra-low ceric dioxide for high-efficiency environmental photocatalysis: organic pollutants degradation and hexavalent chromium reduction, J. Colloid Interface Sci. 601 (2021) 196–208.

[55] C. Qi, X. Liu, J. Ma, C. Lin, X. Li, H. Zhang, Activation of peroxymonosulfate by base: implications for the degradation of organic pollutants, Chemosphere 151 (2016) 280–288.

[56] Y. Wang, Y. Lin, S. He, S. Wu, C. Yang, Singlet oxygen: properties, generation, detection, and environmental applications, J. Hazard. Mater. 461 (2024) 132538.

[57] X. Chen, F. Deng, X. Liu, K.P. Cui, R. Weerasooriya, Hydrothermal synthesis of MnO_2/Fe(0) composites from Li-ion battery cathodes for destructing sulfadiazine by photo-Fenton process, Sci. Total Environ. 774 (2021) 145776.

[58] H. Li, Z. Hu, H. Yu, Photocatalytic degradation of PFOA by hydrangea-like BiOCl with high oxygen vacancies co-mediated under superoxide radicals and holes, J. Environ. Chem. Eng. 11 (2023) 110590.

[59] Z. Fang, Y. Liu, J. Qi, Z.F. Xu, T. Qi, L. Wang, Establishing a high-speed electron transfer channel via CuS/MIL-Fe heterojunction catalyst for photo-Fenton degradation of acetaminophen, Appl. Catal. B Environ. 320 (2023) 121979.

[60] J. Guo, H. Sun, X. Yuan, L. Jiang, Z. Wu, H. Yu, N. Tang, M. Yu, M. Yan, J. Liang, Photocatalytic degradation of persistent organic pollutants by co-cl bond reinforced CoAl-LDH/$Bi_{12}O_{17}Cl_2$ photocatalyst: mechanism and application prospect evaluation, Water Res. 219 (2022) 118558.

[61] M. Wang, G. Lu, R. Jiang, T. Dang, Y. Chen, J. Liu, Z. Yan, J. Hou, Carbon vacancies and spatial confinement effects of VC-$FCN_{0.3}$ prepared by spatial self-corrosion strategy achieved eco-friendly photocatalytic degradation to bisphenol F, J. Clean. Prod. 447 (2024) 141545.

[62] N. Li, R. Li, X. Duan, B. Yan, W. Liu, Z. Cheng, G. Chen, L. Hou, S. Wang, Correlation of active sites to generated reactive species and degradation routes of organics in Peroxymonosulfate activation by co-loaded carbon, Environ. Sci. Technol. 55 (2021) 16163–16174.

[63] H. Zhang, C. Xie, L. Chen, J. Duan, F. Li, W. Liu, Different reaction mechanisms of $\cdot SO_4$- and ·OH with organic compound interpreted at molecular orbital level in co (II)/peroxymonosulfate catalytic activation system, Water Res. 229 (2023) 119392.